CoRuTiGe: A possible spin gapless semiconductor

Ravinder Kumar,[1] Tufan Roy,[2,3] Baisali Ghadai,[4] Rakesh Kumar,[4] Sucheta Mondal,[4] Anil Kumar,[5] Archana Lakhani,[6] Devendra Kumar,[6] Masafumi Shirai,[2,3] and Sachin Gupta[1,*]

[1]*Department of Physics, Bennett University, Greater Noida 201310, India*

[2]*Center for Science and Innovation in Spintronics, Core Research Cluster, Tohoku University, Sendai 980–8577, Japan*

[3]*Research Institute of Electrical Communication, Tohoku University, Sendai 980–8577, Japan*

[4]*Department of Physics, Shiv Nadar Institution of Eminence, Greater Noida 201314, India*

[5]*Department of Physics, Chaudhary Charan Singh University, Meerut-250004 India*

[6]*UGC-DAE Consortium for Scientific Research, University Campus, Khandwa Road, Indore 452001, India*

(Received 12 August 2025; accepted 11 March 2026; published 26 March 2026)

We report experimental and theoretical investigations on the quaternary Heusler alloy CoRuTiGe, synthesized using the arc melting technique. Crystal structure analysis reveals a tetragonal structure at room temperature. Magnetization measurements as a function of temperature and magnetic field indicate a ferromagnetic nature with a saturation magnetization of ∼0.681 μ_B/f.u. at 5 K. The temperature dependence of electrical resistivity shows a nearly linear decrease in the high-temperature range, indicating the spin gapless semiconductor (SGS) like behavior of the material. This SGS nature is further supported by the weak temperature-dependent carrier concentration and mobility. Hall effect analysis reveals that the anomalous Hall effect in CoRuTiGe arises from both intrinsic and extrinsic mechanisms. Additionally, a well-defined symmetric negative magnetoresistance is observed at low temperatures. These results offer insights that could aid in designing new spin gapless semiconductors with enhanced Curie temperatures for spintronic applications.

DOI: 10.1103/l85m-lqqq

I. INTRODUCTION

Spin gapless semiconductors (SGSs) are a new class of quantum materials characterized by a unique electronic band structure, where one spin sub-band exhibits semiconducting behavior, while in the other, the valence and conduction bands touch at the Fermi level, reflecting the gapless nature, as shown in Fig. 1(b) [1–4]. These materials can exhibit quadratic or linear dispersion between energy and momentum [1,2]. Such unique band structures give rise to novel physical properties, making SGSs highly attractive for spintronic applications. The unique band topology of SGSs leads to 100% spin-polarization of both electrons and holes, which is essential for highly efficient spin injection and filtering in devices. Since no energy gap exists for one spin channel, charge carriers can be excited from the valence band to the conduction band with no energy, resulting in extremely low-energy spin transport. In SGSs with linear (Dirac-like) dispersion, the carriers exhibit negligible effective mass, which significantly enhances their mobility compared to conventional semiconductors. Unlike half-metallic ferromagnets (HMFs) [5,6], where one spin subband exhibits semiconducting/insulating behavior, and the other remains metallic as shown in Fig. 1(a), the band structure of spin gapless semiconductors is highly sensitive to external factors such as strain, doping, or electric and magnetic fields. This sensitivity arises because in SGSs, the valence and conduction bands in one spin channel touch at the Fermi level, placing the system at a critical point of a zero band gap [7]. This tunability allows precise control over spin polarization and transport properties, broadening the potential applications of these materials. The capability of controlling spin orientation in the conduction as well as valence bands makes SGSs an ideal candidate for quantum information processing, development of spin-based qubits, quantum Hall effect-based devices, magnetic tunnel junctions, and spintronic memory devices [8–11].

Co-doped $PbPdO_2$ was first predicted to be SGS by X. L. Wang and later realized experimentally [1,12]. The first experimental demonstration of SGS behavior from the Heusler family was reported in an inverse Heusler compound Mn_2CoAl by S. Ouardi *et al.* [13]. SGS materials have been observed to exhibit nearly temperature-independent resistivity or conductivity, characterized by an extremely small temperature coefficient of resistivity (TCR), almost constant carrier concentration across temperatures, and a negligible Seebeck coefficient [13]. Several Heusler alloys have been theoretically predicted to be SGSs; however, only a few have been experimentally confirmed. To fully exploit the potential of this novel class of materials, it is essential to identify new materials and verify their properties experimentally.

In this work, we synthesize a quaternary Heusler alloy CoRuTiGe using the arc melt technique. We study structural, magnetic, and magnetotransport properties experimentally along with some theoretical calculations. The material crystallizes in a tetragonal structure and shows ferromagnetic

*Contact author: sachin.gupta@bennett.edu.in

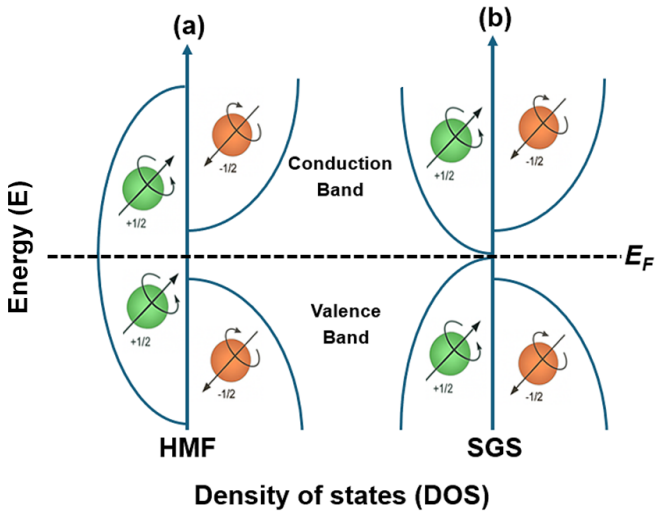

FIG. 1. Density of states (DOS) representation for (a) half metallic ferromagnet (HMF), and (b) spin gapless semiconductor (SGS).

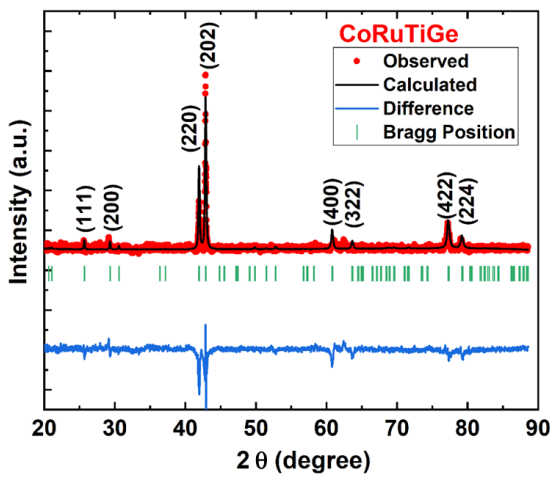

FIG. 2. Room temperature powder x-ray diffraction (XRD) pattern along with Rietveld refinement for CoRuTiGe.

behavior. The temperature and field dependence of electrical resistivity suggest SGS-type behavior in CoRuTiGe.

II. EXPERIMENTAL AND THEORETICAL METHODS

Polycrystalline CoRuTiGe was synthesized under an argon atmosphere using the arc-melt technique. High-purity (at least 99.99%) constituent elements (Co, Ru, Ti, and Ge) were weighed in a stoichiometric ratio of 1:1:1:1 and melted in a water-cooled copper hearth. The sample was melted 4–5 times by flipping it upside down for better homogeneity. To improve the crystal structure, the arc-melted sample was sealed in a quartz tube under high vacuum (up to 10^{-5} mbar) and annealed in a furnace at 850 °C for 7 days. The sample was subsequently quenched in ice water. The crystal structure of the annealed sample was examined using x-ray diffraction (XRD) analysis, performed with Cu Kα radiation ($\lambda = 1.54$ Å) using a Bruker D8 Advance diffractometer at room temperature. Magnetization measurements were carried out using a vibrating sample magnetometer (VSM) associated with Physical Property Measurement System (PPMS), DynaCool, Quantum Design, USA. For transport measurements of CoRuTiGe, a rectangular pellet with dimensions of 6.42 mm $\times$ 4.58 mm $\times$ 1.41 mm was used. Electrical contacts were made using high-conductivity silver paste. The temperature-dependent electrical resistivity (ρ) was measured using the standard linear four-probe method, where a current of 5 mA was applied along the x direction, the voltage drop was measured along the same direction, and the magnetic field was applied perpendicular to the sample plane (along the z direction) using a PPMS system. For Hall effect measurements, a five-probe configuration was employed, with a current of 20 mA applied along the x direction, the magnetic field along the z direction, and the Hall voltage measured in the transverse (y) direction.

First-principles based electronic structure calculations have been performed using projector-augmented-wave method as implemented in Vienna *ab-initio* simulation package (VASP) [14–16]. Generalized gradient approximation (GGA) has been used for the exchange correlation energy/potential [17]. A k mesh of 12 $\times$ 12 $\times$ 12 and a planewave cutoff energy of 520 eV were used for the self-consistent-field calculations. The effect of antisite disorder was studied by considering a 2 $\times$ 2 $\times$ 2 supercell, which includes 32 atoms. The randomness of the swapping disorder was considered by special quasirandom structures (SQS) as implemented in the Alloy Theoretic Automated Toolkit (ATAT) package [18,19]. Furthermore, we evaluate Heisenberg exchange coupling constants using the spin-polarized relativistic Korringa-Kohn-Rostoker package (SPR-KKR) [20]. Here, we used a scalar relativistic potential, which ignores spin-orbit coupling (SOC). Thereafter, we use mean-field approximation to evaluate Curie temperature from the Heisenberg exchange coupling constants using Liechtenstein's formalism [21]. We investigate Berry curvature driven anomalous Hall conductivity (AHC) after constructing a tight-binding Hamiltonian with maximally localized Wannier functions. We used the WANNIER90 code and WANNIERTOOLS for the evaluation of AHC [22–24]. s, p, d orbitals of Co, Ru, and Ti, and s, p, orbitals of Ge were used to construct Wannier functions.

III. RESULTS AND DISCUSSIONS

A. Crystal structure

Figure 2 shows the room temperature XRD pattern in the 2θ range of 20°–90° along with Rietveld refinement. The bottom plot in Fig. 2 shows the difference between experimentally obtained and calculated data. The Rietveld refinement analysis using FullProf suite [25] reveals a tetragonal crystal structure with a space group *P42/nnm* (space group No. 134). The lattice parameters obtained from Rietveld refinement were found to be $a = b = 6.09$ Å and $c = 5.84$ Å. The reason for the transition from the cubic to tetragonal phase could be the stress/strain along the c axis [26]. Various Heusler alloys including $Mn_{3-x}Co_xGa$, $Mn_{3-x}Fe_xGa$, and CoRuTiSn previously have been reported to crystallize in a tetragonal structure [27–29].

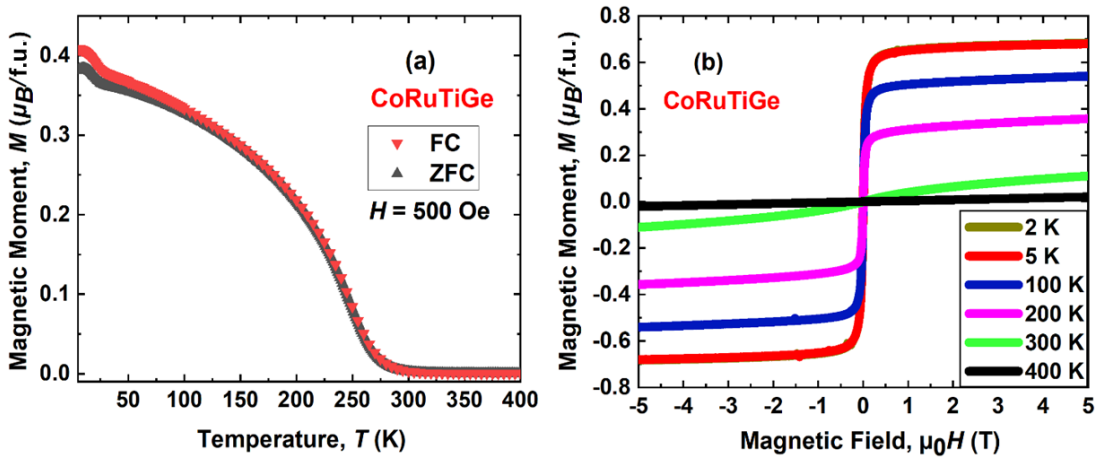

FIG. 3. (a) Temperature, T dependence of magnetization, M in zero field cooling (ZFC) and field cooling (FC) configurations in an applied magnetic field, $H = 500$ Oe. (b) The field, H dependence of magnetization, M as a function of temperature for CoRuTiGe.

B. Magnetic properties

Figure 3(a) shows the temperature, T dependence of magnetization, M, under zero-field-cooled (ZFC) and field-cooled (FC) conditions with an applied field of $H = 500$ Oe for CoRuTiGe. The material exhibits small thermomagnetic irreversibility, along with a slight upturn in magnetization at low temperatures. Such behavior is often associated with magnetic disorder, where competing ferromagnetic and antiferromagnetic interactions, possibly arising from site disorder or antistites defects [30]. The magnetic transition from ferromagnetic to paramagnetic phase is observed near 250 K. Figure 3(b) shows the field-dependent magnetization (M-H) curves at various temperatures (2, 5, 100, 200, 300, and 400 K). The sample exhibits negligible hysteresis, indicating soft ferromagnetic nature of the material. Tetragonal Heusler alloys often exhibit high coercive fields, and this behavior is strongly influenced by the c/a ratio as well as the crystallinity of the sample (single crystalline or polycrystalline) [31–33]. The c/a ratio indicates the deviation of a tetragonal lattice from the ideal cubic symmetry ($c/a = 1$). As this ratio moves away from unity, the lattice becomes elongated or compressed along one axis, which can significantly modify the magnetocrystalline anisotropy [34]. In CoRuTiGe, the tetragonal polycrystalline structure exhibits a c/a ratio of 0.96 (a ∼4% deviation from cubic symmetry), which is relatively small and can reasonably result in the low coercive field observed. Total magnetic moment of a quaternary Heusler alloy can be predicted by the Slater-Pauling (S-P) rule using the following equation [35,36]:

$$M_t = (N_V - 24)\,\mu_B/\text{f.u.}, \tag{1}$$

where M_t is the total magnetic moment and N_V is the total number of valence electrons. CoRuTiGe has 25 valence electrons, therefore, the magnetic moment value is anticipated to be 1 μ_B/f.u. However, the observed value of magnetic moment is found to be ∼ 0.68 μ_B/f.u, deviating from the theoretical prediction by the Slater-Pauling rule (1 μ_B/f.u) [37]. Site disorder, particularly between Co, Ru, and Ti atoms, may induce ferrimagnetic/antiferromagnetic interactions or partial moment compensation, reducing the net magnetic moment.

C. Transport properties

The temperature dependence of electrical resistivity, ρ and conductivity, σ as functions of magnetic field, H is plotted

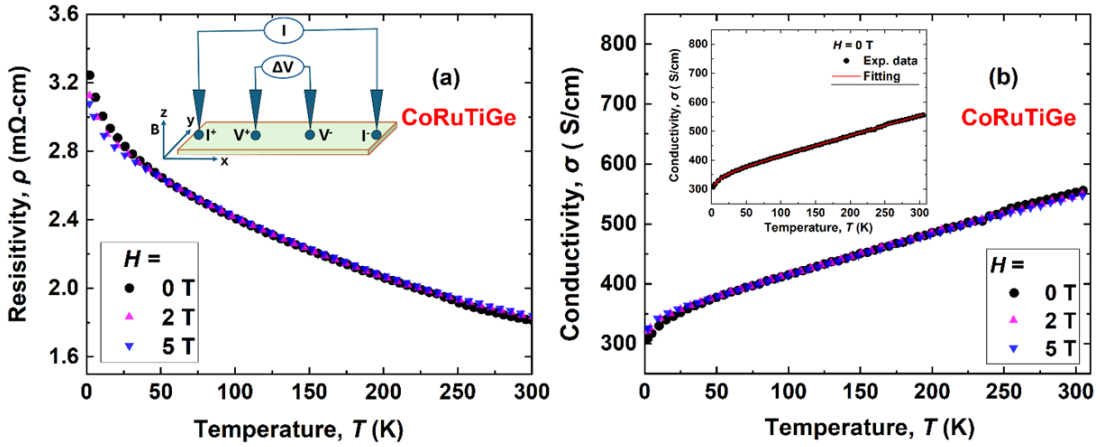

FIG. 4. (a) Temperature T dependence of (a) electrical resistivity ρ and (b) electrical conductivity σ at 0, 2, and 5 T fields for CoRuTiGe. Inset in (a) shows the measurement geometry, and in (b) shows the fitting of conductivity data using Eq. (3).

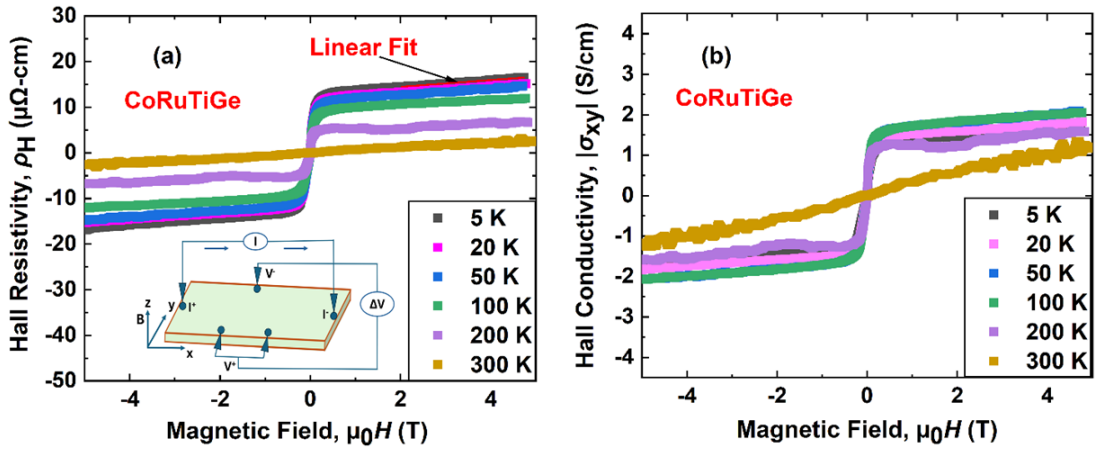

FIG. 5. The field dependence of (a) the Hall resistivity ρ_H. Inset of (a) shows the schematic of measurement geometry and (b) the Hall conductivity $|\sigma_{xy}|$ as a function of temperature for CoRuTiGe.

in Figs. 4(a) and 4(b), respectively. As seen in Fig. 4(a), the resistivity decreases nearly linear with increasing temperature in the range of 50–300 K. However, this behavior is distinct from that of conventional semiconductors, which typically exhibit an exponential decrease in resistivity with temperature [13]. The magnitude of resistivity at 300 K is about 1.8 mΩ cm and is comparable to the magnitude of CoFeCrAl (0.8 mΩ cm), previously reported SGS [38]. The linear decrease in resistivity with temperature corresponds to a negative temperature coefficient of resistivity (TCR) of approximately -3.3×10^{-6} Ω cm/K, which falls within the typical range observed in other spin gapless semiconductors

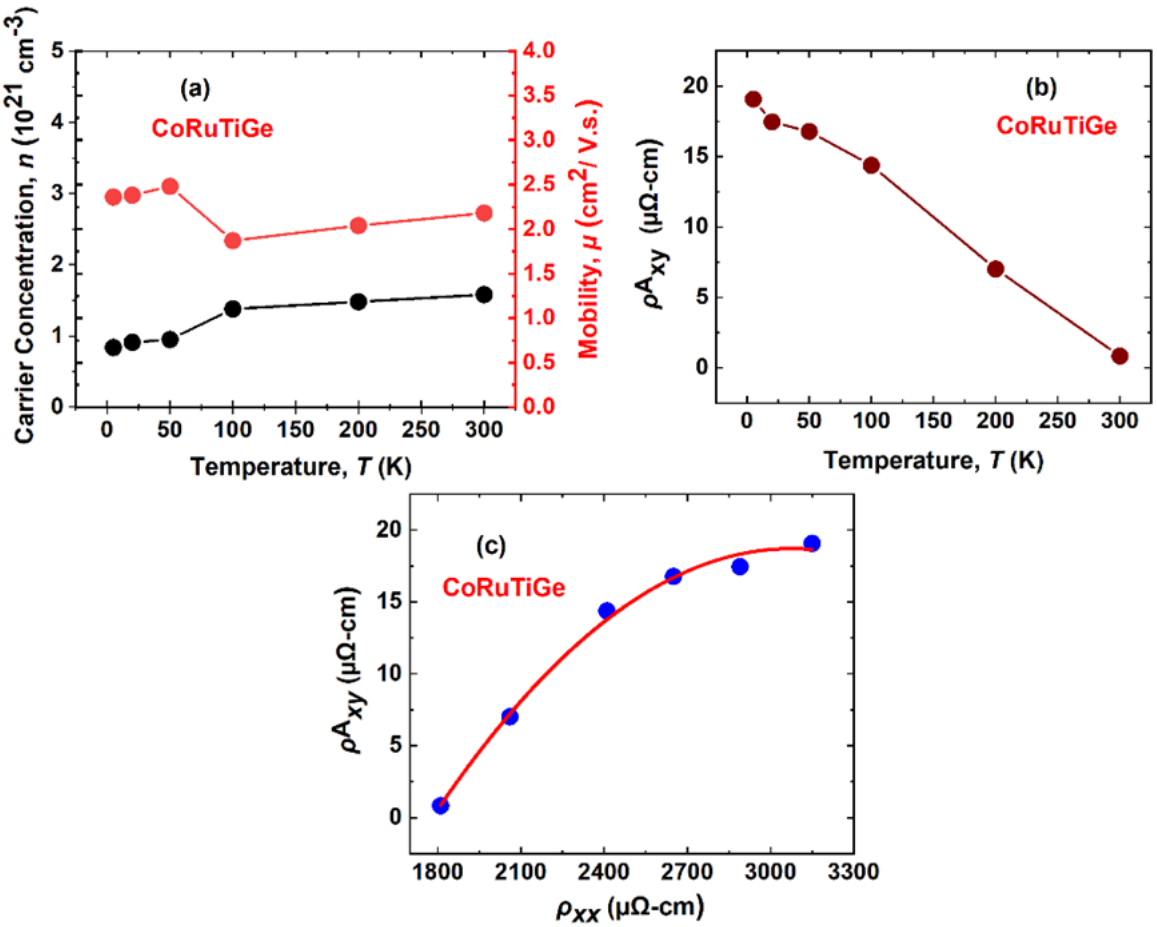

FIG. 6. Temperature dependence of (a) charge carrier concentrations, n and (b) anomalous Hall resistivity ρ^A_{xy}. (c) anomalous Hall resistivity ρ^A_{xy} vs longitudinal resistivity ρ_{xx} and the solid red line shows the fitting of data by Eq. (6).

such as Mn_2CoAl [13], CoFeCrGa [39], and CoFeCrAl [38]. These observations suggest spin gapless semiconductor–type behavior in CoRuTiGe.

To understand the electrical transport properties of CoRuTiGe, the conductivity data were analyzed using the two-carrier model proposed by Kharel *et al.* [38]. This model has been successfully used to describe the conductivity behavior of various narrow-gap, gapless semiconductors as well as disordered SGSs. The conductivity was fitted using an equation that includes contributions from both the gapless spin channel (σ_{SGS}) and the semiconducting channel (σ_{SC}).

$$\sigma(T) = \sigma_{SGS} + \sigma_{SC}. \tag{2}$$

The above equation can be rewritten as [38,40]

$$\sigma\ (T) = \sigma_o\left[1 + 2\ln(2)\frac{K_B T}{g}\right] + \sigma_{SC0}\exp\left(\frac{-\Delta E}{K_B T}\right). \tag{3}$$

Here σ_o is the gapless conductivity at 0 K, σ_{SC0} is the semiconducting contribution at 0 K, K_B is the Boltzmann constant, ΔE is the activation energy, and g is a parameter reflecting the overlapping of bands or deviation from the ideal SGS state, including disorder. Equation (3) was fitted to experimental conductivity data, and the parameters obtained from the fitting were found to be $\sigma_o = 310.83$ S/cm, $\sigma_{SC0} = 40.19$ S/cm, $g = 54.4$ meV, and $\Delta E = 0.99$ meV [inset Fig. 4(b)]. The value of g indicates an overlap between the conduction and valence bands in the majority spin subband. This suggests a deviation from the ideal spin gapless semiconductor behavior, where no band overlap is expected. Such an approach has previously been used to analyze disordered SGS systems, where band overlap arises due to structural disorder or intrinsic defects within the material. The *g value,* therefore, suggests the presence of disorder-induced modifications in the band structure of CoRuTiGe [38,40].

D. Hall effect

Hall measurements for CoRuTiGe were carried out as a function of temperature and magnetic field up to 5 T, applied perpendicular to the sample plane as shown in Fig. 5(a). A five probe contact method was used for Hall effect measurement [41]. Measurement geometry is shown in the inset of Fig. 5(a). In ferromagnetic materials, the transverse resistivity typically includes both ordinary and anomalous Hall contributions. The total Hall resistivity ρ_H can be expressed as [42]

$$\rho_H = R_o\mu_0 H + R_s M. \tag{4}$$

Here, the first term represents the ordinary Hall contribution, while the second term corresponds to the anomalous Hall contribution. R_o and R_s are the ordinary and anomalous Hall coefficients, respectively, and μ_0 is the permeability of free space.

The Hall conductivity $|\sigma_{xy}|$ of the sample can be calculated using the following relation [43]:

$$|\sigma_{xy}| \cong \frac{\rho_H}{\rho_{xx}^2}, \tag{5}$$

where ρ_{xx} is the longitudinal resistivity. The Hall conductivity, $|\sigma_{xy}|$ calculated using Eq. (5), is shown in Fig. 5(b). The charge carrier concentration, n at different temperatures was estimated by linear fitting of the Hall resistivity data at high magnetic fields and was found to be of the order of $\sim 10^{21}$ cm^{-3}. Both the carrier concentration and mobility in CoRuTiGe exhibit weak temperature dependence as shown in Fig. 6(a), which might be attributed to the overlapping of majority bands at the Fermi level. Similar temperature dependence has been reported in other SGS materials [44–46]. To extract the anomalous Hall resistivity, ρ_{xy}^A the y intercept of the linear extrapolation of the high-field region of the Hall resistivity curve was used. The temperature dependence of ρ_{xy}^A shown in Fig. 6(b), exhibits a trend similar to that of the zero-field longitudinal resistivity.

The anomalous Hall effect (AHE) is primarily governed by two distinct mechanisms: An intrinsic mechanism, which originates from the Berry curvature of the electronic band structure, and an extrinsic mechanism, which arises from impurity scattering [47]. The extrinsic contribution can be further divided into two types of scattering processes: Skew scattering and side-jump. Skew scattering is linearly proportional to longitudinal resistivity ρ_{xx} and results from asymmetric scattering of charge carriers due to impurities. In contrast, the side-jump mechanism is attributed to local distortions of the electronic wave function caused by impurity potentials, which generate a lateral displacement and thus a localized current density. Differentiating between the side-jump and intrinsic (Berry curvature) contributions is challenging, as both scale with ρ_{xx}^2. The overall scaling behavior of the anomalous Hall resistivity can be described by the empirical relation [48]

$$\rho_{xy}^A = a\rho_0 + b(\rho_{xx} - \rho_0) + c\rho_{xx}^2, \tag{6}$$

where ρ_0 is the residual resistivity. The coefficients a and b correspond to skew scattering contributions from defect-induced and phonon-induced scattering, respectively, while c accounts for the combined intrinsic (Berry curvature) and side-jump effects. Figure 6(c) shows the fitting of ρ_{xy}^A using Eq. (6), yielding the following parameters: $a = 0.041$, $b = 0.068$, and $c = -1.116 \times 10^{-5}$ $(\mu\Omega\,\text{cm})^{-1}$. The results

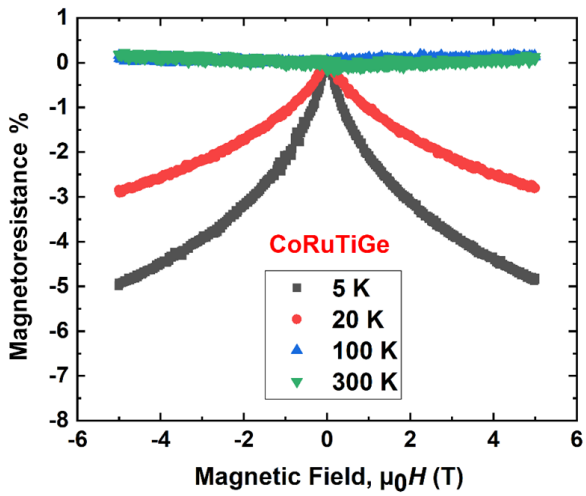

FIG. 7. The field dependence of magnetoresistance, MR at 5, 20, 100, and 300 K temperature for CoRuTiGe.

TABLE I. Considered configurations of the atomic arrangement in CoRuTiGe.

Configuration	A	B	C	D	Energy (eV/f.u.)
	(0, 0, 0)	(0.5, 0.5, 0.5)	(0.25, 0.25, 0.25)	(0.75, 0.75, 0.75)	
Type 1	Co	Ru	Ti	Ge	0
Type 2	Co	Ti	Ru	Ge	1.678
Type 3	Co	Ge	Ru	Ti	1.133

clearly indicate that the AHE in CoRuTiGe arises from a combination of intrinsic and extrinsic mechanisms. The value of b is found to be larger than a, suggesting that phonon-induced skew scattering is the dominant extrinsic mechanism. Additionally, the small value of c indicates a minor contribution from Berry curvature, i.e., the intrinsic mechanism plays a limited role in this sample. Similar trends have been observed in other materials such as CoFeMnSn [44] CoFeMnSi film [46], and Mn_2CoAl film [49].

E. Magnetoresistance

Magnetoresistance (MR) refers to the change in a material's electrical resistance in response to an external magnetic field and is calculated using the following equation [50]:

$$\text{MR } \% = \frac{R(T,H) - R(T,0)}{R(T,0)} \times 100, \tag{7}$$

where R is an electrical resistance. Magnetic fields up to ± 5 T was used to record the change in resistance at 5, 20, 100, and 300 K temperatures as shown in Fig. 7. At low temperatures (5 and 20 K), the material exhibits a nonsaturating, symmetric negative MR of up to 5%. In ferromagnetic materials, such negative MR typically arises from the suppression of spin-dependent scattering with increasing magnetic field [51]. However, at higher temperatures, the change in resistance with applied magnetic field becomes negligible.

F. Theoretical results

1. Crystal structure and stability

In quaternary Heusler alloys with space group $F\bar{4}3m$, there are four atomic sites, A (0, 0, 0), B (0.5, 0.5, 0.5), C (0.25, 0.25, 0.25), D (0.75, 0.75, 0.75). We considered three different types of configurations as described in Table I and compared their total energies with respect to the type 1. Notably, a type-1 configuration is the most stable, and therefore, the type-2 and type-3 configurations are excluded from further discussion. The optimized lattice parameter of the type-1 configuration is 5.986 Å, which is consistent with earlier reports based on first-principles investigations [37].

As there has not been any prior report on the experimental synthesis of CoRuTiGe. So, it is important to discuss the stability of CoRuTiGe in terms of the formation energy ΔE and the phase separation energy δE. Negative ΔE stands for the stability of an alloy against decomposition into bulk phases of the constituent elements, whereas negative δE indicates that the alloy is not likely to segregate to form any other secondary alloys. Formation energy of CoRuTiGe is -0.57 eV/atom. The phase separation energy is $+0.08$ eV/atom. Note that we considered ternary Heusler alloys, such as Co_2TiGe and Ru_2TiGe as the competing phases. Earlier studies support that the alloys with a marginally positive phase separation energy (<0.1 eV/atom) is synthesizable in experiment [52,53].

2. Electronic structure of ordered phase

Figure 8 presents the spin-resolved band dispersion and density of states (DOS) for CoRuTiGe in its perfectly ordered, Y structure. It has a half-metallic electronic structure owing to the presence of a band gap of 0.35 eV in the minority spin channel. On the other hand, the top of the valence band just touches the Fermi level, resulting in a pseudogap and a very small DOS in the majority spin channel at the Fermi level. Thus CoRuTiGe can be considered as a nearly spin gapless semiconductor in its ordered

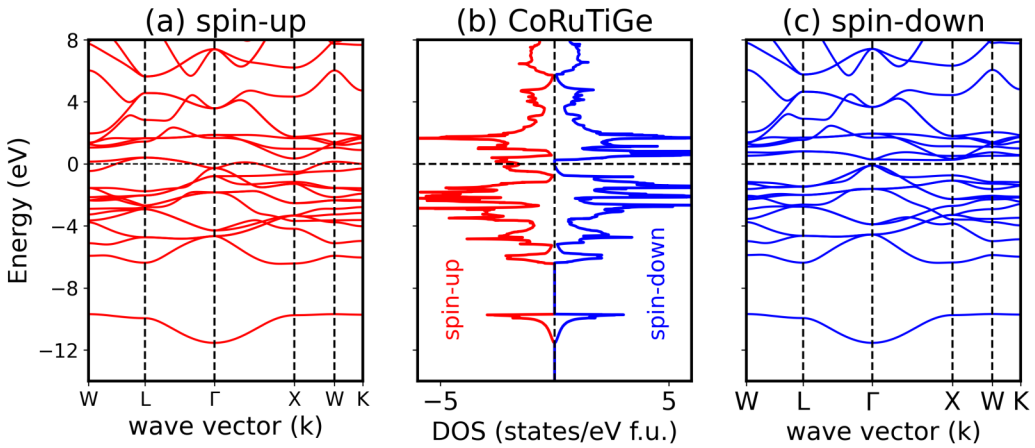

FIG. 8. Spin-resolved band structure and density of states (DOS) of ordered CoRuTiGe.

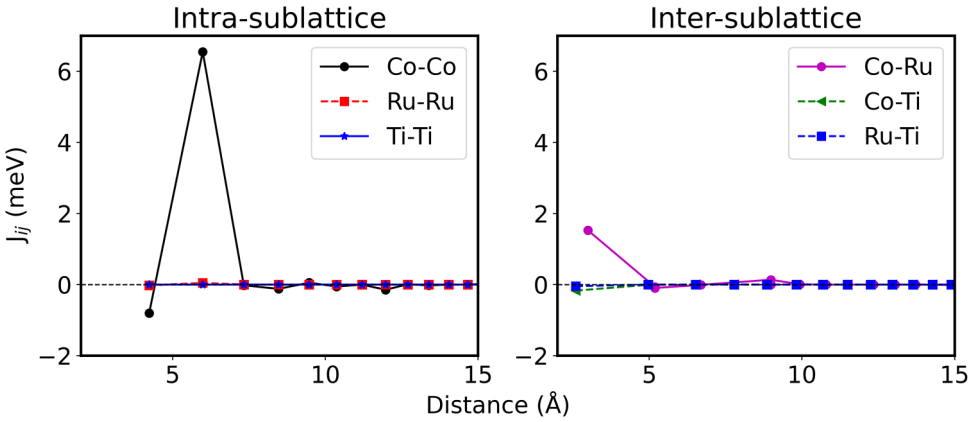

FIG. 9. Heisenberg exchange coupling parameters as a function of interatomic distance.

structure. The scenario is quite similar to our earlier investigation on the isoelectronic, quaternary Heusler alloy CoRuTiSn [29].

3. *Magnetic moment and Heisenberg exchange coupling constant*

Calculated total magnetic moment of CoRuTiGe is 1.00 μ_B, which satisfies the Slater-Pauling rule [54]. Co, Ru, Ti, and Ge atoms carry a magnetic moment of 0.86 μ_B, 0.21 μ_B, -0.03 μ_B, 0 μ_B, respectively. Now to understand the magnetic interactions between the constituent elements, we present Heisenberg exchange coupling constants (J_{ij}) between the ith and jth atoms as a function of the interatomic distance (R_{ij}) in Fig. 9 for the ordered phase. The positive (negative) values of J_{ij} represent ferromagnetic (antiferromagnetic) interactions between ith and jth atoms. Noting that Co is the element with the largest magnetic moment in CoRuTiGe, the strongest interaction is between Co atoms themselves, which is a long-range oscillatory RKKY type of interaction. Although, the stronger interaction between Co atoms is limited up to the second nearest neighbor or the boundary first unit cell (∼6 Å), however, a weak Co-Co interaction is extended beyond the second unit cell (∼12 Å). Other magnetic interactions are between Co and Ru, Co and Ti, and Ru and Ti atoms. These interactions are reasonably weak. We also evaluate the Curie temperature based on the mean-field-approximation, which is about 230 K, which is close to the experimentally observed value.

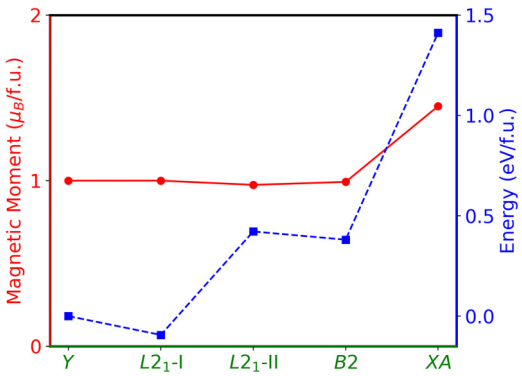

FIG. 10. Total magnetic moment and total energy for the ordered and disordered structures.

4. *Stability of swapping disorder and its impact on electronic structure*

In the experimental synthesis of quaternary Heusler alloys, it is indeed a challenge to fabricate an ordered phase or Y-type structure, because of possible antistite disorders. These antistite disorders could impact the electronic structure as well as the magnetism. In this section, we discuss the stability of the formation of disorders resulting from site exchange of the constituent atoms. Figure 10 shows a comparison of the total energies and magnetic moments after considering a number of possible site exchanges, such as between (i) Co and Ru ($L2_1-$I), (ii) Ti and Ge ($L2_1-$II), (iii) Co and Ru, and Ti and Ge, simultaneously ($B2$), and (iv) Ru and Ti atoms (XA).

We find that in all cases except XA type, the total magnetic moment remains very close to 1.00 μ_B, thus not sensitive to the disorders. However, in XA type, the total magnetic moment

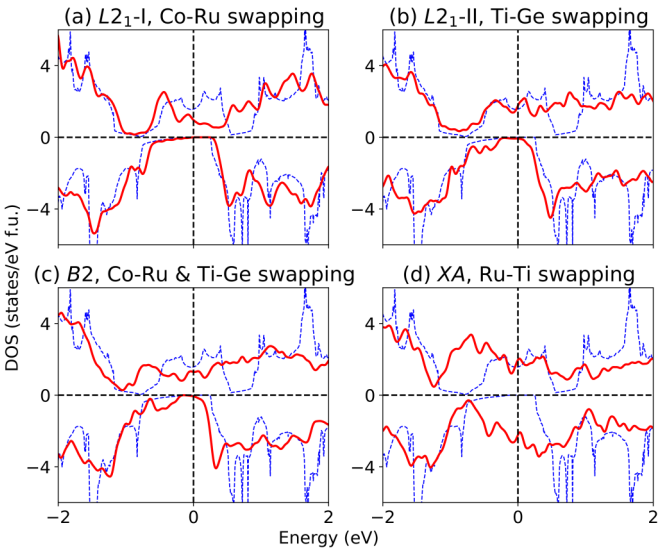

FIG. 11. Solid red lines show the density of states for the disordered phases. The dashed blue line shows the density of states for the ordered phase.

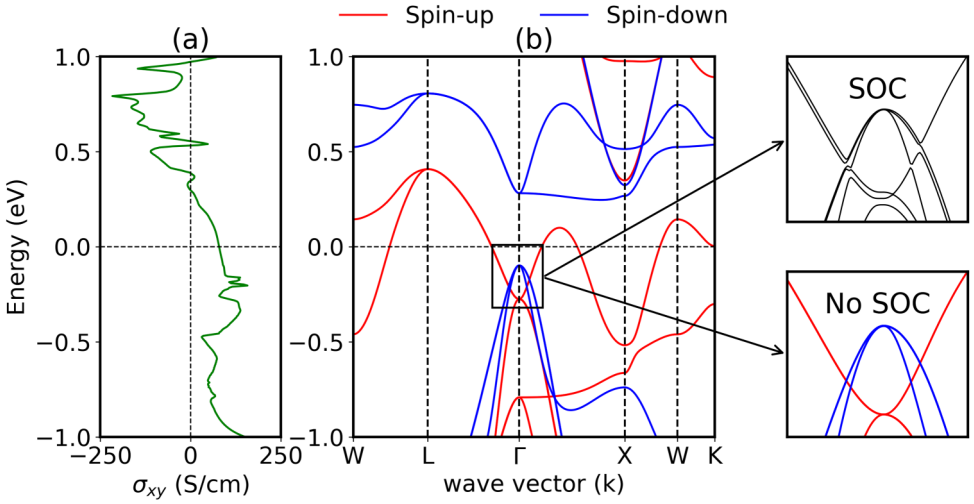

FIG. 12. (a) Anomalous Hall conductivity as a function of Fermi energy. (b) Spin-resolved band dispersion. Insets show zoomed-in views of the rectangular box marked in (b). The top inset shows the band dispersion in the presence of SOC, while the bottom inset, in the absence of SOC.

becomes 1.45 μ_B. Now, we compare the relative stability of the respective disordered phases with respect to the ordered one in terms of total energies. We find that $L2_1-$I (–0.093 eV/f.u.) is the energetically most favorable, followed by *Y* (0 eV/f.u.), *B*2 (+0.380 eV/f.u), $L2_1-$II (+ 0.422 eV/f.u.) types of structures. It is to note that *XA* type (+1.411 eV) is energetically the most unfavorable, thus least likely to be synthesized in experiment.

Figure 11 shows the impact of different swapping disorders on the DOS. In each case, the DOS of the disordered one (Red solid line) is compared with that of the ordered one (broken blue line). We find that the DOS around the Fermi level is least affected by the swapping of Co and Ru atoms, namely $L2_1-$I, type of disorder. Half-metallicity is maintained in all types of disorders except *XA*-type, which involves the swapping of Ru and Ti atoms.

5. Anomalous Hall conductivity

In Fig. 12(a), we present the anomalous Hall conductivity (AHC) σ_{xy} as a function of the Fermi energy position. We find that at the Fermi energy, $\sigma_{xy} = 79$ S/cm which is much larger than the experimental value. Note that the calculational value is obtained for the ordered structure of the *Y* type. We could also observe a peak value of $\sigma_{xy} = 150$ S/cm at about 0.2 eV below the E_F. This peak value corresponds to the band crossing between spin-up and spin-down bands near the Γ point as enclosed by the rectangular box in Fig. 12(b). We also present the zoomed-in view of the rectangular box in the presence and in the absence of SOC as marked by the arrows. We find that the consideration of SOC leads to band anticrossings at the points where spin-up and spin-down bands intersect each other.

These band anticrossings act as the source of Berry curvature and of intrinsic AHC in the presence of SOC [55]. Thus we believe successful fabrication of ordered structure, along with the tuning of the Fermi level position at about –0.2 eV in terms of the hole doping could significantly enhance the intrinsic contribution to the AHC.

G. Discussions

In this work, the structural, magnetic, and electrical properties of the quaternary Heusler alloy CoRuTiGe were investigated through a combined first-principles calculations and experimental measurements. The theoretical calculations were performed for the ideal cubic Y-type structure as well as for several antisite-disorder configurations commonly observed in quaternary Heusler alloys [38,56–58]. These calculations provide a reference framework for understanding the intrinsic electronic and magnetic behavior of an ordered system and enable comparison with the experimentally observed results.

Experimentally, however, the synthesized CoRuTiGe sample crystallizes in a tetragonal structure rather than the expected cubic phase. This deviation is likely caused by internal strain or lattice distortion introduced during the synthesis process. The magnetic and transport properties of this tetragonal phase were analyzed to assess their deviation from theoretical expectations. For the ordered cubic structure, the calculated density of states (DOS) indicates a half-metallic or nearly spin gapless semiconducting character with a total magnetic moment of ~ 1 μ_B/f.u., consistent with the Slater-Pauling rule. Among all the calculated configurations, the $L2_1-$I phase (–0.093 eV/f.u.) was found to be the most stable and satisfied the same rule.

In contrast, the experimentally obtained magnetic moment is significantly smaller. To address this issue, we discuss the impact of tetragonality and local magnetic-moment ordering. We considered a 16-atom unit cell instead of the four-atom primitive unit cell shown in Fig. 13. The 16-atom unit cell contains four atoms each of Co, Ru, Ti, and Ge. Note that Co is the primary magnetic-moment-carrying atom in the unit cell.

We compared the total energies of two magnetic configurations: (i) ferromagnetic configuration (FM) in which all Co magnetic moments are aligned parallel to each other, and (ii) ferrimagnetic configuration (FiM) in which one out of the four Co atoms has an antiparallel spin orientation with respect to the other three Co atoms. We find that the latter

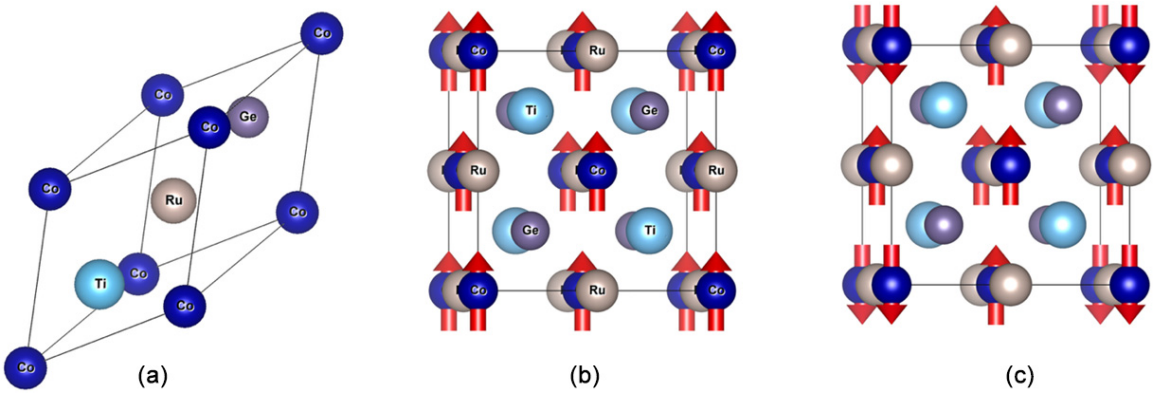

FIG. 13. (a) Four-atom primitive fcc unit cell. 16-atom P1 unit cell with (b) ferromagnetic and (c) ferrimagnetic configurations. Arrows indicate the directions of the spin magnetic moment vector of Co atoms.

configuration is marginally more favorable than the ferromagnetic one by 6 meV/f.u. The resulting total magnetic moment is 0.52 μ_B/f.u., which is much closer to the experimentally obtained value of 0.68 μ_B/f.u.

In the previous section, the theoretical calculation of σ_{xy} was performed for the ordered *Y*-type cubic structure. Now to address the experimentally obtained σ_{xy} value, which is significantly lower than the theoretical prediction, we calculated the same for the tetragonal structure with the ferrimagnetic (FiM) configuration as described earlier. Figure 14 demonstrates the comparison between the calculated σ_{xy} of the ordered fcc structure and that of the tetragonal structure evaluated with experimental lattice parameters. We find that the value of σ_{xy} at the Fermi level is reduced to 55 S/cm. Moreover, just above the Fermi level (+0.03 eV), σ_{xy} exhibits a pronounced dip to approximately 10 S/cm. Thus, it is plausible that charge doping arising from defects or disorder in the experimental sample could shift the Fermi level by a small amount, leading to such a significant reduction in σ_{xy}. This reduction is consistent with the strong sensitivity of AHC to Berry curvature, which is diminished when band crossings near the Fermi level are shifted or smeared due to disorder and structural distortion [13,59,60].

Overall, these findings demonstrate that atomic disorder and lattice distortion have a profound impact on the electronic, magnetic, and topological properties of CoRuTiGe. To realize the full potential of this alloy for spintronic applications, further optimization—such as elemental substitution, strain engineering, or refined synthesis and annealing protocols—may be required to stabilize the ideal structure and enhance its functional properties.

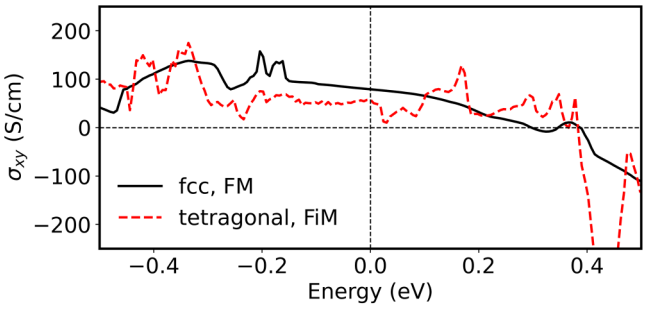

FIG. 14. Anomalous Hall conductivity as a function of the Fermi energy for CoRuTiGe in the ferrimagnetic (FiM) state with experimental lattice parameters (broken red line) and in the ferromagnetic (FM) fcc structure (solid black line).

IV. CONCLUSIONS

The quaternary Heusler alloy CoRuTiGe was synthesized using the arc melt technique. The crystal structure from the XRD pattern was found to be tetragonal. The material shows a ferromagnetic to paramagnetic magnetic transition with negligible hysteresis and saturation magnetization of $\sim$ 0.681 μ_B/f.u. at 5 K. The resistivity decreases linearly with temperature, and the temperature-independent carrier concentration and mobility suggest spin gapless semiconductorlike behavior of CoRuTiGe. It shows negative MR with the field at low temperatures, which becomes negligible at room temperature. Our calculations reveal a clear deviation of the magnetic moment from its Slater–Pauling integer value, attributable to the ferrimagnetic ground state. Furthermore, the results highlight the strong sensitivity of the anomalous Hall conductivity to structural distortions. Overall, these results provide useful insights that can guide the design of new spin gapless semiconductors with improved Curie temperatures, thereby advancing their potential for spintronic applications.

ACKNOWLEDGMENTS

The authors sincerely thank K. G. Suresh, IIT Bombay, for experimental support in material synthesis and Amitabh Das for insightful discussions. S.G. gratefully acknowledges the financial support from the Anusandhan National Research Foundation (ANRF), New Delhi, under Project No. SUR/2022/004713 for facilitating this research work. B.G. would like to acknowledge Shiv Nadar Institution of Eminence, Delhi NCR for the fellowship. This work was in part supported by the Initiative to Establish Next-Generation Novel Integrated Circuit Centers (X-NICS) (Grant No. JPJ011438) from the Ministry of Education, Culture, Sports, Science and Technology (MEXT), and by the Center for Science and Innovation in Spintronics (CSIS), Tohoku University.

DATA AVAILABILITY

The data that support the findings of this article are not publicly available upon publication because it is not technically feasible and/or the cost of preparing, depositing, and hosting the data would be prohibitive within the terms of this research project. The data are available from the authors upon reasonable request.

[1] X. L. Wang, Proposal for a new class of materials: Spin gapless semiconductors, Phys. Rev. Lett. **100**, 156404 (2008).

[2] X. L. Wang, S. X. Dou, and C. Zhang, Zero-gap materials for future spintronics, electronics and optics, npj Asia Mater. **2**, 31 (2010).

[3] X. Wang, Z. Cheng, J. Wang, X. L. Wang, and G. Liu, Recent advances in the Heusler based spin-gapless semiconductors, J. Mater. Chem. C **4**, 7176 (2016).

[4] R. Kumar and S. Gupta, Novel Heusler materials for spintronic applications: Growth, characterizations and applications, arXiv:2504.17742.

[5] A. Q. Seh and D. C. Gupta, Quaternary Heusler alloys a future perspective for revolutionizing conventional semiconductor technology, J. Alloys Compd. **871**, 159560 (2021).

[6] R. Kumar and S. Gupta, Experimental realization of CoFeRuSn quaternary Heusler alloy for room temperature spintronic applications, Appl. Phys. Lett. **124**, 022402 (2024).

[7] L. Bainsla, A. I. Mallick, M. M. Raja, A. K. Nigam, B. S. D. C. S. Varaprasad, Y. K. Takahashi, A. Alam, K. G. Suresh, and K. Hono, Spin gapless semiconducting behavior in equiatomic quaternary CoFeMnSi Heusler alloy, Phys. Rev. B **91**, 104408 (2015).

[8] M. Nadeem and X. Wang, Spin gapless quantum materials and devices, Adv. Mater. **36**, 2402503 (2024).

[9] Q. Sun, Y. Ma, and N. Kioussis, Two-dimensional Dirac spin-gapless semiconductors with tunable perpendicular magnetic anisotropy and a robust quantum anomalous Hall effect, Mater. Horizons **7**, 2071 (2020).

[10] Z. Yue, Z. Li, L. Sang, X. Wang, Z. Yue, Z. Li, L. Sang, and X. Wang, Spin-gapless semiconductors, Small **16**, 1905155 (2020).

[11] X. Wang, Z. Cheng, G. Zhang, H. Yuan, H. Chen, and X. L. Wang, Spin-gapless semiconductors for future spintronics and electronics, Phys. Rep. **888**, 1 (2020).

[12] X. Wang, G. Peleckis, C. Zhang, H. Kimura, and S. Dou, Colossal electroresistance and giant magnetoresistance in doped $PbPdO_2$ thin films, Adv. Mater. **21**, 2196 (2009).

[13] S. Ouardi, G. H. Fecher, C. Felser, and J. Kübler, Realization of spin gapless semiconductors: The Heusler compound Mn_2CoAl, Phys. Rev. Lett. **110**, 100401 (2013).

[14] P. E. Blöchl, Projector augmented-wave method, Phys. Rev. B **50**, 17953 (1994).

[15] G. Kresse and J. Furthmüller, Efficient iterative schemes for ab initio total-energy calculations using a plane-wave basis set, Phys. Rev. B **54**, 11169 (1996).

[16] G. Kresse and D. Joubert, From ultrasoft pseudopotentials to the projector augmented-wave method, Phys. Rev. B **59**, 1758 (1999).

[17] J. P. Perdew, K. Burke, and M. Ernzerhof, Generalized gradient approximation made simple, Phys. Rev. Lett. **77**, 3865 (1996).

[18] A. Zunger, S.-H. Wei, L. G. Ferreira, and J. E. Bernard, Special quasirandom structures, Phys. Rev. Lett. **65**, 353 (1990).

[19] A. van de Walle, P. Tiwary, M. de Jong, D. L. Olmsted, M. Asta, A. Dick, D. Shin, Y. Wang, L.-Q. Chen, and Z.-K. Liu, Efficient stochastic generation of special quasirandom structures, Calphad **42**, 13 (2013).

[20] H. Ebert, D. Ködderitzsch, and J. Minár, Calculating condensed matter properties using the KKR-Green's function method—recent developments and applications, Rep. Prog. Phys. **74**, 096501 (2011).

[21] A. I. Liechtenstein, M. I. Katsnelson, V. P. Antropov, and V. A. Gubanov, Local spin density functional approach to the theory of exchange interactions in ferromagnetic metals and alloys, J. Magn. Magn. Mater. **67**, 65 (1987).

[22] N. Marzari and D. Vanderbilt, Maximally localized generalized Wannier functions for composite energy bands, Phys. Rev. B **56**, 12847 (1997).

[23] I. Souza, N. Marzari, and D. Vanderbilt, Maximally localized Wannier functions for entangled energy bands, Phys. Rev. B **65**, 035109 (2001).

[24] Q. Wu, S. Zhang, H.-F. Song, M. Troyer, and A. A. Soluyanov, WannierTools: An open-source software package for novel topological materials, Comput. Phys. Commun. **224**, 405 (2018).

[25] J. Rodriguez-Carvajal, Recent advances in magnetic structure determination neutron powder diffraction, Phys. B **192**, 55 (1993).

[26] P. Wang, J. B. Xia, and H. Bin Wu, Electronic structures, magnetic properties and strain effects of quaternary Heusler alloys FeMnCrZ (Z = P, As, Sb, Bi, Se, Te), J. Magn. Magn. Mater. **490**, 165490 (2019).

[27] C. Felser, V. Alijani, J. Winterlik, S. Chadov, and A. K. Nayak, Tetragonal Heusler compounds for spintronics, IEEE Trans. Magn. **49**, 682 (2013).

[28] Z. H. Liu, Z. J. Tang, J. G. Tan, Y. J. Zhang, Z. G. Wu, X. T. Wang, G. D. Liu, and X. Q. Ma, Tailoring structural and magnetic properties of $Mn_{3-x}Fe_xGa$ alloys towards multifunctional applications, IUCrJ **5**, 794 (2018).

[29] R. Kumar, T. Roy, M. Shirai, and S. Gupta, Low-moment semiconducting properties of quaternary Heusler alloy CoRuTiSn, J. Alloys Compd. **1026**, 180530 (2025).

[30] B. Govind, P. Bharti, S. Bano, A. Kumar, S. Singh, and V. P. S. Awana, Disorder induced magnetic behavior of non-stoichiometric $Co_{0.75}Mn_{0.5}Fe_{0.75}Si$ full-Heusler alloy, J. Supercond. Nov. Magn. **35**, 445 (2022).

[31] A. K. Nayak, C. Shekhar, J. Winterlik, A. Gupta, and C. Felser, Mn_2PtIn: A tetragonal Heusler compound with exchange bias behavior, Appl. Phys. Lett. **100**, 152404 (2012).

[32] Y. You, G. Xu, F. Hu, Y. Gong, E. Liu, G. Peng, and F. Xu, Designing magnetic compensated states in tetragonal Mn_3Ge-based Heusler alloys, J. Magn. Magn. Mater. **429**, 40 (2017).

[33] Q. Ma, A. Sugihara, K. Suzuki, X. Zhang, T. Miyazaki, and S. Mizukami, Tetragonal Heusler-like Mn-Ga alloys based perpendicular magnetic tunnel junctions, Spin **04**, 1440024 (2014).

[34] L. Wollmann, S. Chadov, J. Kübler, and C. Felser, Magnetism in tetragonal manganese-rich Heusler compounds, Phys. Rev. B **92**, 064417 (2015).

[35] J. C. Slater, The Ferromagnetism of Nickel, Phys. Rev. **49**, 537 (1936).

[36] L. Pauling, The nature of the interatomic forces in metals, Phys. Rev. **54**, 899 (1938).

[37] S. Bahramian and F. Ahmadian, Half-metallicity and magnetism of quaternary Heusler compounds CoRuTiZ (Z = Si, Ge, and Sn), J. Magn. Magn. Mater. **424**, 122 (2017).

[38] P. Kharel, W. Zhang, R. Skomski, S. Valloppilly, Y. Huh, R. Fuglsby, S. Gilbert, and D. J. Sellmyer, Magnetism, electron transport and effect of disorder in CoFeCrAl, J. Phys. D. Appl. Phys. **48**, 245002 (2015).

[39] A. Chanda, D. Rani, D. DeTellem, N. Alzahrani, D. A. Arena, S. Witanachchi, R. Chatterjee, M. H. Phan, and H. Srikanth, Large thermo-spin effects in Heusler alloy-based spin gapless semiconductor thin films, ACS Appl. Mater. Interfaces **15**, 53697 (2023).

[40] S. Dixit, S. Ghosh, S. Mishra, N. Shahi, P. Shahi, S. Singh, A. K. Bera, S. M. Yusuf, Y. Uwatoko, C.-F. Chang, and S. Chatterjee, Effect of antisite disorder on the magnetic and transport properties of a quaternary Heusler alloy, arXiv:2410.20673.

[41] D. Rani, L. Bainsla Enamullah, K. G. Suresh, and A. Alam, Spin-gapless semiconducting nature of Co-rich $Co_{1+x}Fe_{1-x}CrGa$, Phys. Rev. B **99**, 104429 (2019).

[42] S. Gupta, S. Kanai, F. Matsukura, and H. Ohno, Magnetic and transport properties of Sb_2Te_3 doped with high concentration of Cr, Appl. Phys. Express **10**, 103001 (2017).

[43] X. D. Xu, Z. X. Chen, Y. Sakuraba, A. Perumal, K. Masuda, L. S. R. Kumara, H. Tajiri, T. Nakatani, J. Wang, W. Zhou, Y. Miura, T. Ohkubo, and K. Hono, Microstructure, magnetic and transport properties of a Mn_2CoAl Heusler compound, Acta Mater. **176**, 33 (2019).

[44] S. Gupta, J. Sau, M. Kumar, and C. Mazumdar, Spin-gapless semiconducting characteristics and related band topology of quaternary Heusler alloy CoFeMnSn, J. Mater. Chem. C **12**, 706 (2024).

[45] H. Fu, Y. Li, L. Ma, C. You, Q. Zhang, and N. Tian, Structures, magnetism and transport properties of the potential spin-gapless semiconductor CoFeMnSi alloy, J. Magn. Magn. Mater. **473**, 16 (2019).

[46] V. Mishra, V. Barwal, L. Pandey, N. Kumar Gupta, S. Hait, A. Kumar, N. Sharma, N. Kumar, and S. Chaudhary, Investigation of spin gapless semiconducting behaviour in quaternary CoFeMnSi Heusler alloy thin films on Si (1 0 0), J. Magn. Magn. Mater. **547**, 168837 (2022).

[47] N. Nagaosa, J. Sinova, S. Onoda, A. H. MacDonald, and N. P. Ong, Anomalous Hall effect, Rev. Mod. Phys. **82**, 1539 (2010).

[48] Y. Tian, L. Ye, and X. Jin, Proper scaling of the anomalous hall effect, Phys. Rev. Lett. **103**, 087206 (2009).

[49] N. Y. Sun, Y. Q. Zhang, H. R. Fu, W. R. Che, C. Y. You, and R. Shan, Perpendicular magnetic anisotropy in Mn_2CoAl thin film, AIP Adv. **6**, 015006 (2016).

[50] S. Gupta, K. G. Suresh, and A. K. Nigam, Observation of large positive magnetoresistance and its sign reversal in GdRhGe, J. Alloys Compd. **586**, 600 (2014).

[51] B. Bandyopadhyay, J. Nag, S. Paul, M. K. Chattopadhyay, A. Lakhani, A. Alam, and K. G. Suresh, Griffiths phase-like behavior in nearly half-metallic CoFeVAl: Theory and experiment, Phys. Rev. B **109**, 094433 (2024).

[52] Q. Gao, I. Opahle, and H. Zhang, High-throughput screening for spin-gapless semiconductors in quaternary Heusler compounds, Phys. Rev. Mater. **3**, 024410 (2019).

[53] T. Tsuchiya, T. Roy, K. Elphick, J. Okabayashi, L. Bainsla, T. Ichinose, K. Z. Suzuki, M. Tsujikawa, M. Shirai, A. Hirohata, and S. Mizukami, Magnetic tunnel junctions with a B2-ordered CoFeCrAl equiatomic Heusler alloy, Phys. Rev. Mater. **3**, 084403 (2019).

[54] I. Galanakis, P. H. Dederichs, and N. Papanikolaou, Slater-Pauling behavior and origin of the half-metallicity of the full-Heusler alloys, Phys. Rev. B **66**, 174429 (2002).

[55] K. Manna, L. Muechler, T.-H. Kao, R. Stinshoff, Y. Zhang, J. Gooth, N. Kumar, G. Kreiner, K. Koepernik, R. Car, J. Kübler, G. H. Fecher, C. Shekhar, Y. Sun, and C. Felser, From colossal to zero: Controlling the anomalous hall effect in magnetic Heusler compounds via berry curvature design, Phys. Rev. X **8**, 041045 (2018).

[56] Y. Venkateswara Enamullah, S. Gupta, M. R. Varma, P. Singh, K. G. Suresh, and A. Alam, Electronic structure, magnetism, and antisite disorder in CoFeCrGe and CoMnCrAl quaternary Heusler alloys, Phys. Rev. B **92**, 224413 (2015).

[57] P. Kharel, J. Herran, P. Lukashev, Y. Jin, J. Waybright, S. Gilbert, B. Staten, P. Gray, S. Valloppilly, Y. Huh, and D. J. Sellmyer, Effect of disorder on the magnetic and electronic structure of a prospective spin-gapless semiconductor MnCrVAl, AIP Adv. **7**, 056402 (2017).

[58] D. Rani, L. Bainsla, K. G. Suresh, and A. Alam, Experimental and theoretical investigation on the possible half-metallic behaviour of equiatomic quaternary Heusler alloys: CoRuMnGe and CoRuVZ (Z = Al, Ga), J. Magn. Magn. Mater. **492**, 165662 (2019).

[59] N. Shahi, A. K. Jena, G. K. Shukla, V. Kumar, S. Rastogi, K. K. Dubey, I. Rajput, S. Baral, A. Lakhani, S. C. Lee, S. Bhattacharjee, and S. Singh, Antisite disorder and Berry curvature driven anomalous Hall effect in the spin gapless semiconducting Mn_2CoAl Heusler compound, Phys. Rev. B **106**, 245137 (2022).

[60] S. Rastogi, V. Kumar, A. K. Jena, N. Shahi, G. K. Shukla, S. W. D'Souza, S. Bhattacharjee, and S. Singh, Atomic disorder and intrinsic anomalous Hall effect in a half-metallic ferromagnet Co_2VAl, J. Alloys Compd. **1010**, 177212 (2025).